

Spectrally- and Temporally-Resolved Optical Depth Measurements in High Explosive Post-Detonation Fireballs

Rylie Lodes,^{*,[a]} Herman Krier,^[a] and Nick Glumac^[a]

Abstract: Temporally-and-spectrally-resolved-optical-depth-measurements were made in fireballs from five common high explosives. Chambered explosive detonations were probed with 405 nm, 532 nm, 650 nm, 1310 nm, and 9600 nm laser light to quantify optical attenuation during the first 5 ms after initiation. Attenuation lengths are reported for each wavelength and high explosive as a function of time. Two charge sizes were studied to show optical depth scaling for charge mass. Trends in optical depth be-

tween type of explosive and probe wavelength are presented and discussed. The spectral dependence of attenuation departed strongly from the λ^4 prediction from Rayleigh scattering, indicating significant absorption in addition to scattering. Beam steering effects were determined to be of minimal influence for the scale of explosives tested. Blast scaling is considered in attempt to generalize the results presented.

Keywords: Optical Depth • Laser Attenuation • Detonator • High Explosive • Explosive Fireball

1 Introduction

Optical diagnostics are common diagnostic tools that researchers can employ to study high explosive detonations and post-detonation fireballs due to their non-invasive nature. Pyrometry, emission and absorption spectroscopy, and photometry, among other techniques, all rely on light traveling through or out of the fireball. Explosive fireballs tend to be optically dense, and the interpretation of emission measurement in terms of spatial averaging remains uncertain. Light emitted from an optically thick fireball can be scattered so significantly that only light from the outermost regions of the fireball reaches the observer, biasing spectral emission measurements. Fireballs with high optical density emit as a thermal greybodies, whereas less opaque fireballs show increased spectral dependence on emissivity. This difference complicates the processing of emission data, as a priori knowledge of emissivity for constituent species must be known for the complex, multiphase flow and increases uncertainty in temperature measurements.

Optical depth is often discussed in the context of the challenges it poses researchers or the limitations it places on optical data from post-detonation high explosive fireballs. Previous studies have discussed the impact optical depth has on the interpretation of optical diagnostic data, citing not only the broadband attenuation of light, but also self-absorption of chemical species and increased uncertainty in temperature fitting [1]. Lewis et al. compared visible emission spectra collected both outside and inside aluminized HMX explosive fireballs, illustrating that path-averaged optical diagnostics on optically thick fireballs provide misleading data [2]. The emitted intensity from the fireballs was found to be largely inconsistent at various

depths from the fireball surface. Carney et al. used PETN as their base explosive due to its optical clarity post-detonation for early time optical absorption work [3]. Some work in the area of optical depth quantification in the explosive environment has been completed, however there still is little information on the impact of explosive composition and wavelength dependence. Peuker et al. investigated the temporal and spatial dependence on optical depth in aluminized explosive fireballs from 50 mg charges. Early-time attenuation lengths of 532 nm laser light were found to be less than 1 cm during the luminous portion of the fireball, with a subsequent reduction in optical density after 160 μ s post-detonation [4].

Following the detonation of a high explosive, products are generally very fuel-rich with significant amounts of hydrocarbon species, CO, and soot. Fireball radiation is primarily from the hot, condensed phase products in the post-detonation mixture. Fireball conditions can vary markedly from the outer edge, where oxidation reactions involving ambient oxygen primarily occur, to the inside where pyrolysis tends to dominate. The amount of condensed phase in a fireball affects its opacity significantly, and thus oxygen balance of an explosive is likely to be a key factor in the optical depth of a particular fireball [5].

[a] R. Lodes, H. Krier, N. Glumac
Mechanical Science and Engineering
University of Illinois at Urbana-Champaign
Mechanical Engineering Laboratory, 105 S. Matthews Avenue, Urbana, Illinois, 61801
*e-mail: ryliel2@illinois.edu
glumac@illinois.edu

Agglomerated combustion products, along with soot, attenuate light as it pass through this multiphase environment. Reduction of light intensity through a medium is quantified by extinction, the sum of absorption and scattering through a participating medium. Extinction follows the Beer-Lambert law, defined by Hanson as [6]:

$$A_\nu = 1 - \exp(-k_\nu L) = 1 - \left(\frac{I}{I_0}\right) \quad (1)$$

Where κ_ν is the spectral absorption coefficient, L is the path length through the medium, and their product is the optical depth. The optical depth is a measure of the optical opacity, or optical density, of the medium and quantifies how much light is absorbed and scattered as it traverses a medium. It is common to express optical depth in terms of attenuation length, with dimensions of centimeters. This characteristic length is the thickness through a slab of gas that transmits $1/e$, or about 37%, of the original light intensity through to the observer. In other words, attenuation length is the path length the beam must travel through a medium for the optical depth to equal unity. Hence, it follows that:

$$k_\nu = -\frac{\ln\left(\frac{I}{I_0}\right)}{L} \quad (2)$$

$$k_\nu L_{att} = -\ln\left(\frac{1}{e}\right) = 1 \rightarrow L_{att} = \frac{1}{k_\nu} = -\frac{L}{\ln\left(\frac{I}{I_0}\right)} \quad (3)$$

If the optical depth is much smaller than unity, the optically thin approximation is likely applicable for the medium. Furthermore, fireballs much smaller than the characteristic attenuation length can likely be considered optically thin. However, it remains to be shown under what explosive conditions and wavelength ranges this is the case.

In the present work, we provide quantitative, spectrally and temporally resolved optical depth data in fireballs from PBXN-5 (95% HMX, 5% fluoroelastomer), composition A-5 (99% RDX, 1% stearic acid), Primasheet 1000 (65% PETN, 8% nitrocellulose, 27% plasticizer), PETN, and composition A-5 mixed with 20 weight percent aluminum powder. Information on the explosives used in the experiments are detailed in Table 1. These explosives are common formulations to which optical diagnostics are often applied, and optical depth quantification would be helpful in the design of future experiments. Small scale (125 mg, 250 mg) explosive pellets were initiated with an 80 mg PETN initiating charge and probed with 405 nm, 532 nm, 650 nm, 1310 nm, and 9600 nm laser light. The spectral region chosen for this study covers much of the region of interest for both spectral emission and absorption measurements from explosive fireballs and post-detonation products. We expect these data to be valuable in showing to what degree of op-

tical depth can be expected for a certain explosive, distance from the charge center, time after initiation, and wavelength. The data presented herein will help guide researchers in designing optical experiments, aid in the understanding of optical data collected from the explosive events, and provide a better understanding of the influences of explosive type and wavelength on optical depth.

2 Experimental Section

Explosive charges were detonated in air in a 2.18 L closed explosive testing chamber fitted with windows for optical access. Quartz windows on one axis provide optical transmission of the 405 nm, 532 nm, 650 nm, 1310 nm lasers, and imaging, while zinc selenide (AR coated at 8–12 μm) windows on the second optical axis allow for transmission of the 9600 nm laser light. Photodiodes (ThorLabs DET36 A Si biased detectors) fitted with 25 mm focal length plano-convex lenses and color filters (Roscolux #59, #388, #19) were used to detect the 405 nm, 532 nm, and 650 nm laser light. The photodiode used to detect the 1310 nm laser light (ThorLabs DET10 C InGaAs biased detector) was fitted with an interference filter (1310 nm center wavelength (CWL) with 10 nm FWHM) and a 25 mm focal length plano-convex lens. The addition of the lenses to the photodiodes serves to reduce the impact of beam steering of the laser light through the density gradients produced by the detonation and turbulent mixing of post-detonation gases. Two masses of output explosive were tested, 125 mg and 250 mg, and the explosive train was a modified RP-80 exploding bridgewire (EBW) detonator made by Teledyne RISI. A gold bridge wire initiates an 80 mg pellet of low-density PETN which then initiates the chosen output pellet. In the 250 mg charges, two 125 mg output pellets are stacked and bonded with a thin layer of cyanoacrylate. Figure 1 shows a schematic of the charge configuration employed in the experiments.

Figure 2 shows the high explosive chamber testing chamber. The laser beams pass through a common point directly above the charge surface. The long-wave infrared laser beam passes through the bottom zinc selenide win-

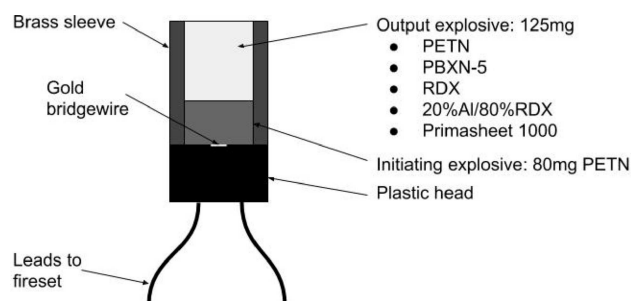


Figure 1. Schematic of charge used in experiments. Output high explosive and mass were varied.

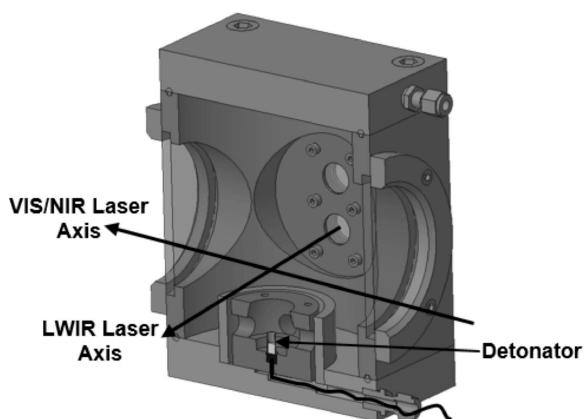


Figure 2. Cutaway CAD rendering of the explosive blast chamber. Detonator is shown in center.

dows. The detonator sits in the steel cup in the center of the chamber.

Figure 3 shows an image sequence obtained by a High-Speed Framing Camera (HSFC) of the early fireball expansion from 125 mg of RDX. The fireball starts as a cone as it expands upward toward the top of the chamber. As the fireball reaches the top of the chamber it swirls outward toward the walls before flowing down the sides of the chamber. When fireball cools, the swirling induced by the encounter with the top of the chamber mixes the post-detonation products as the flow comes to a rest. Fireball luminosity is shown from high-speed imaging to subside approximately 3 ms post-detonation for the 125 mg charges and approximately 2 ms post-detonation for the 250 mg charges.

Long-wave infrared radiation was provided by a 40 Watt carbon dioxide laser. Most of the output power from the laser was dumped into a beam dump while approximately 1% of the beam was picked off by the front surface reflection of an angled zinc selenide window at a slight angle of incidence. The long-wave infrared beam was then directed through the explosive test chamber to an infrared grating monochromator. The monochromator was coupled

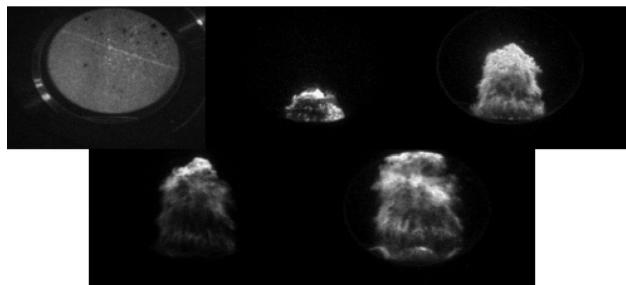


Figure 3. Early-time fireball evolution from the detonation of 125 mg RDX. Left to right, top to bottom: Pre-shot, $t + 20 \mu\text{s}$, $t + 25 \mu\text{s}$, $t + 35 \mu\text{s}$, $t + 45 \mu\text{s}$.

with a mercury-cadmium-telluride DC-coupled infrared detector (Vigo VS3 PVM-10.6-1x1) which selected and monitored the P-branch of the CO_2 bend near $9.6 \mu\text{m}$ emitted by the carbon dioxide laser.

The 405 nm, 532 nm, and 650 nm laser light was provided by 10 mW laser diodes with $\pm 10 \text{ nm}$ CWL. These laser diodes were mounted on kinematic mounts to accurately adjust the directionality of the beams. The 1310 nm laser was a tunable diode laser manufactured by QPhotonics (QDFBLD-1300-5). The output of the laser was a FC/PC collimated fiber optic mounted on a kinematic mount to maintain alignment relative to the other lasers. A schematic of the experimental setup is shown in Figure 4.

The beams were arranged such that all beams intersected at a common interrogation point in the center of the chamber 7.5 cm above the charge in the center of the chamber. Beam diameters were between 2–5 mm circular beam profiles at the intersection point. Care was taken to ensure the path length each beam took through the chamber was comparable, with less than 1 cm deviation. Despite the difference in path lengths, transmission and absorbance calculations consider each individual path length to provide direct comparison of beam attenuation along each respective path length. Properties of each laser can be seen in Table 2. Path lengths for the first $120 \mu\text{s}$ were approximated as the fireball diameter obtained from the high-speed imaging. Afterwards, the path length through the chamber for each laser was used, and are shown in Table 2.

Care was taken to reduce the impact of beam steering on the optical depth experiments. Beam steering is the

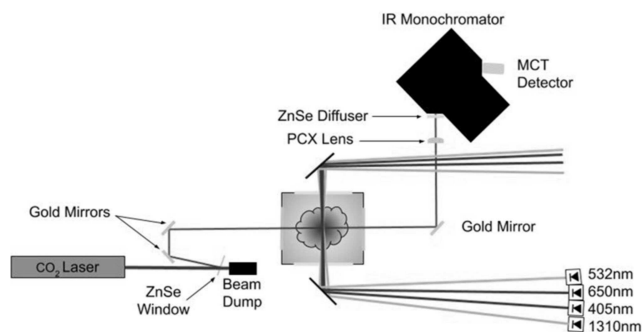


Figure 4. Schematic of experimental setup.

Table 1. High explosive formulations used in the experiments and their oxygen balances.

High Explosive	Chemical Formula	Oxygen Balance
PETN	$\text{C}_5\text{H}_8\text{N}_4\text{O}_{12}$	−10.12 %
PBXN-5 (95 % HMX)	$\text{C}_4\text{H}_8\text{N}_8\text{O}_8$	−21.61 %
RDX	$\text{C}_3\text{H}_6\text{N}_6\text{O}_6$	−21.61 %
Primasheet 1000		
65 % PETN	$\text{C}_5\text{H}_8\text{N}_4\text{O}_{12}$	−10.12 %
8 % Nitrocellulose	$\text{C}_{18}\text{H}_{21}\text{N}_{18}\text{O}_{38}$	−13.61 %

phenomenon by which a laser beam direction is changed due to a change in index of refraction of the transmitting medium. The explosive fireball and hot combustion gases present an inhomogeneous density field which tends to

distort the beam path through the chamber. In attempt to quantify this effect, we set up a beam steering experiment for both sizes of explosive charge. One beam was passed through the chamber and the photodiode was replaced by a Chronos 1.4 high-speed camera operating at 16 kHz at 2 μ s exposure imaging the laser spot on a diffuser screen. However, the beam did not displace from the pre-shot position by more than half the beam diameter, indicating that the beam steering effects are negligible compared to the optical attenuation from the fireball with the addition of the lenses on the photodiodes.

Table 2. Properties of lasers used in the experiments.

Laser Wavelength (nm)	Path Length (cm)	Beam Diameter (mm)
405	12.71	3
532	12.73	3
650	12.72	4
1310	12.70	2
9600	13.29	5

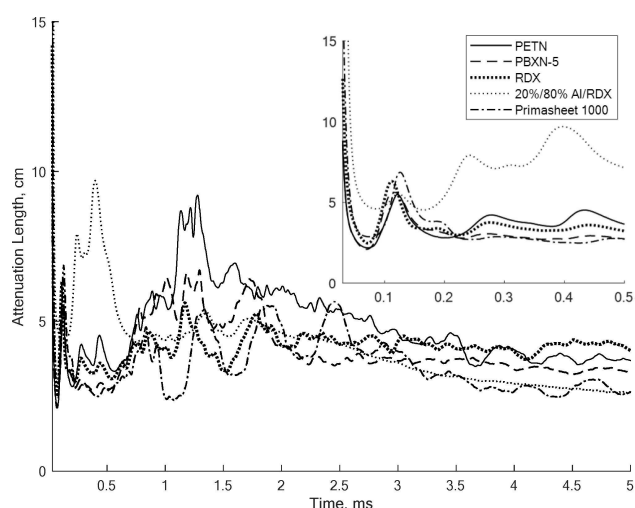


Figure 5. 405 nm laser attenuation length as a function of time for 125 mg charges.

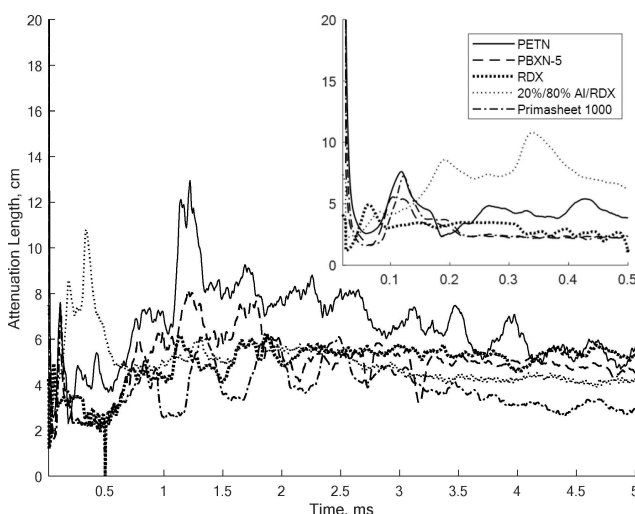


Figure 6. 532 nm laser attenuation length as a function of time for 125 mg charges.

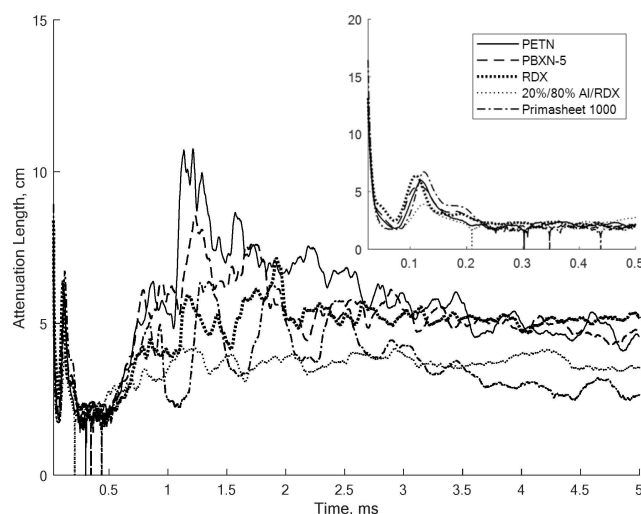


Figure 7. 650 nm laser attenuation length as a function of time for 125 mg charges.

3 Results and Discussion

Characteristic attenuation length data are shown for each wavelength plotted against time for each explosive tested in Figures 5–9. The plots start approximately 30 μ s after charge initiation, as significant electrical interference was present prior to that time. No meaningful data is truncated since the fireball arrives at the common interrogation point in the 25–30 μ s timeframe. In-figure zooms show the first 500 μ s of data. Transmission was calculated by taking I_0 as an average of the first 1 ms of data pre-trigger and dividing transmitted intensity I by this reference. Intrinsic fireball luminosity was strongly rejected by both spatial and spectral filtering. The quartz output window was fitted with a mask which only had a small hole to allow the lasers to pass through it, and blocked the majority of the fireball luminosity. Additionally, the photodiodes were placed a distance away from the chamber such any luminosity escaping the pinhole of the mask was expanded sufficiently to not detect emission signal on the photodiodes through the spectral filters. The light on the detectors were checked to be below saturation before each test to ensure attenuations meas-

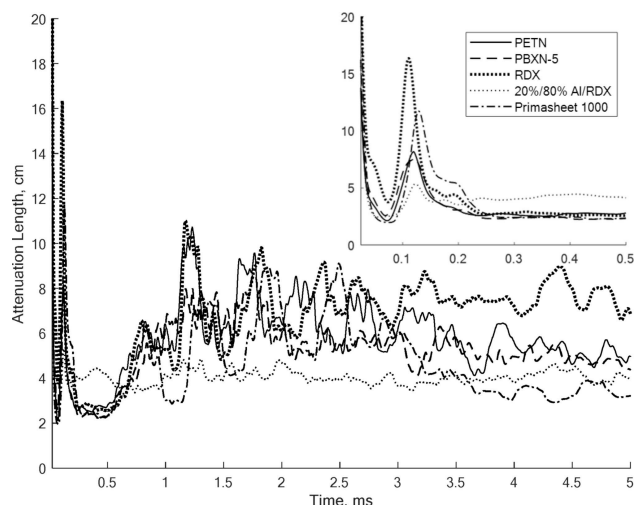


Figure 8. 1310 nm laser attenuation length as a function of time for 125 mg charges.

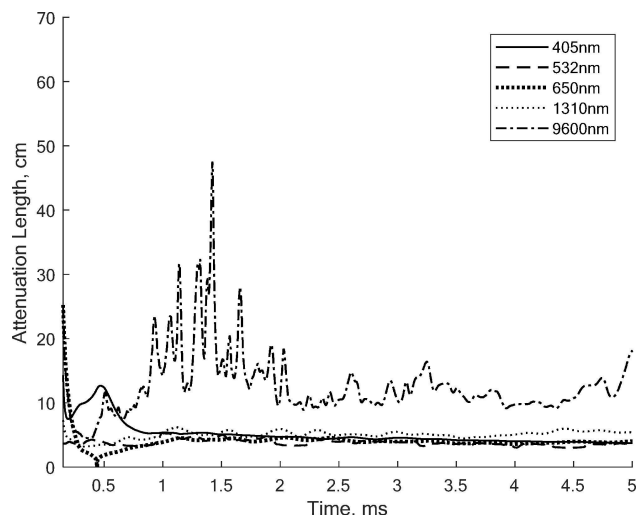


Figure 10. Attenuation lengths as a function of time for a 250 mg RDX charge. Note change in axis scaling.

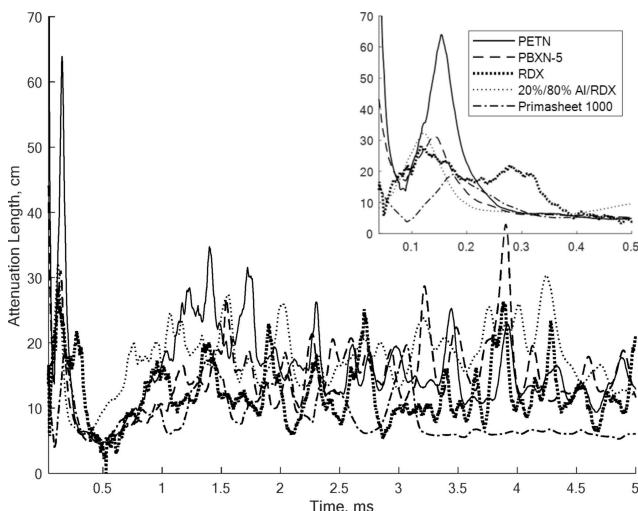


Figure 9. 9600 nm laser attenuation length as a function of time for 125 mg charges. Note change in axis scaling.

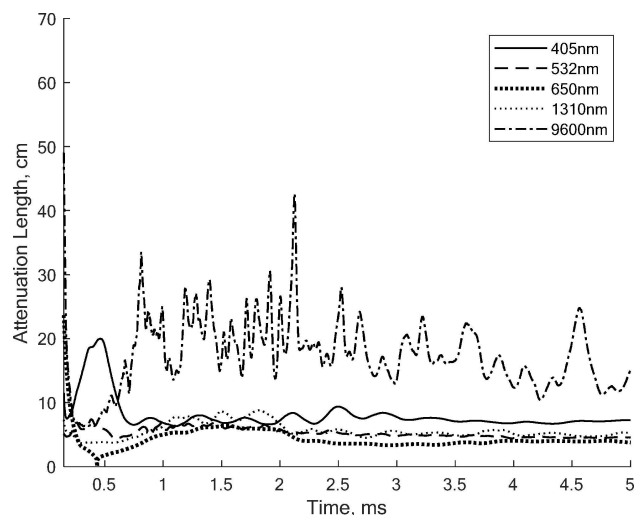


Figure 11. Attenuation lengths as a function of time for a 250 mg PETN charge. Note change in axis scaling.

ured were representative of the fireball. Optical depths and attenuation lengths were calculated using Eqs. 2 and 3, respectively, and plotted against time. Attenuation length is the depth through a scattering and participating medium by which the transmitted intensity is $1/e$, or approximately 37%, of the original intensity. Figures 10 and 11 show the attenuation length as a function of time for the 250 mg RDX and PETN charges.

An important observation from these data is that the entire event, for visible through near-infrared wavelengths, attenuation lengths were shorter than the fireball diameter. The long-wave infrared attenuation length peaks near 500 μs and was approximately equal to the fireball diameter; however, for this size explosive, attenuation length was nearly 50% longer after this period. This result implies that

the optical depth effects on measurements made in the visible to near-infrared during the entire event will have a strong impact, whereas the environment will be significantly less opaque in the first 500 μs for long-wave infrared light measurements during an explosive event. Peuker et al. investigated the early-time attenuation length in aluminized RDX up to 160 μs post-detonation, citing characteristic lengths of several centimeters for the first 100 μs , and tens of centimeters near 160 μs [4]. The data presented herein correlates well with their findings; however, the period after 100 μs appeared thicker compared to Peuker's data, though Peuker's setup was unconfined, allowing for further expansion and thinning of product gases. Other observed differences could be due to the location of measure-

ment relative to the explosive charge, since a variation in optical density with spatial location was noted in that study.

Close to 1 ms after detonation, an increase in attenuation length is shown. The decrease in optical density could be due to the relative measurement location with respect to the fireball center. Since the fireball is growing and moving upward toward the top of the chamber, the probe location of the lasers relative to the fireball center changes, and could lead to temporal fluctuations in attenuation length due to spatial variations in opacity. After the fireball luminosity subsides, nearly 2–3 ms post-detonation, attenuation lengths decreased steadily as the fireball combustion products filled the chamber and settled out. The deposition of combustion products on the chamber windows could be a reason for the observed decrease in attenuation length as the products circulate through the chamber.

PETN presented the longest attenuation length among tested explosives following the early period of high reactivity and optical density. Peak attenuation lengths were close to 10 cm for the visible through NIR wavelengths, while the long-wave infrared peaked at over 60 cm. PETN has an oxygen balance of -10.21% , which indicates it has a greater ability to self-oxidize and burn more completely compared to the other explosives investigated. The ability to burn more completely reduces the soot production and leaves less particulate to scatter and absorb the laser light. After the luminous period of the fireball, however, the attenuation length was approximately equivalent to those of the RDX and PBXN-5 charges.

PBXN-5 presented longer attenuation lengths relative to RDX during the period of fireball luminosity, despite having equivalent oxygen balance at -21.61% for the constituent high explosives. Nevertheless, PBXN-5 attenuation lengths were typically several centimeters longer than RDX in this regime. After the period of fireball luminosity, RDX presented longer attenuation lengths in the visible through NIR wavelengths, albeit modestly. Far-infrared attenuation lengths for PBXN-5 were roughly equivalent to RDX for the first 1 ms before becoming much longer than RDX for the remainder the data collection window. From nearly 1 ms onward, the difference in attenuation length between PBXN-5 and RDX was approximately 10 cm, which is an appreciable difference for the scale of explosives tested.

Aluminization of RDX decreases the attenuation length relative to RDX by several centimeters. However, the attenuation length of the aluminized RDX composition at early time was the longest among tested high explosives. After this period, the attenuation length was among the shortest relative to the tested explosives. Comparing the relative attenuation lengths between RDX and the aluminized RDX composition shows that metallizing high explosives has a significant impact of the optical properties of the fireball.

Primasheet 1000 presented the shortest attenuation length among the high explosives tested. Due to its relatively high composition of binder and plasticizer, Prima-

sheet 1000 produces large amounts of soot when it detonates and attenuates the beams substantially. The soot produced by Primasheet 1000 was evidenced by the thick black soot deposits in the chamber after test. Attenuation lengths for Primasheet 1000 were a factor of 2–3 shorter than neat PETN, indicating that the addition of plasticizer to explosive compositions impacts the optical properties of the explosive fireballs greatly and decreases the characteristic attenuation length.

Comparing the attenuation lengths among high explosives for each wavelength reveals a spectral dependence on attenuation through the fireball. Near-infrared and far-infrared radiation is attenuated significantly less than the visible radiation wavelengths studied. Attenuation length was nearly longer than 10 cm or more for every high explosive tested besides Primasheet 1000 after the early time reactivity ($t < 500 \mu\text{s}$) for 9600 nm laser light. Near-infrared 1310 nm laser light attenuation length was above 5 cm for the majority of tests. Laser attenuation length increased as wavelength increased, trending with predictions from scattering theory, however the spectral dependence shown is weaker than the λ^{-4} dependence predicted by single scattering in the Rayleigh limit alone. This reduced spectral dependence implies that there is simultaneous absorption along the pathlength, in addition to single scattering and, perhaps, multiple scattering. Furthermore, the particular size distribution of combustion products and condensed phase species may tend away from regimes for which the simple Rayleigh case is applicable. To explain the spectral dependence, a deeper look into the fireball chemistry is required. Post-detonation fireballs are extremely complex multiphase flows with large amounts of gas and condensed phase species. The gas phase species will likely not contribute to the absorption of the specific lasers employed in this experiment, and will mainly interact with the laser beams by scattering, typically in the Rayleigh limit of small scattering diameter. The condensed phase products will interact by scattering and absorbing the incident radiation which has been extensively studied in common combustion systems.

In hydrocarbon flames, the condensed phase species are predominantly carbonaceous particles produced from incomplete oxidation. Reactions between small radicals and larger hydrocarbon radicals produce polycyclic aromatic hydrocarbons (PAHs), which are a known precursor to soot. PAHs combine to form nascent primary soot particles with diameters in the 10–50 nm range. As soot matures, the primary particles grow by surface addition, aggregation (tightly bound primary particles), and agglomeration (loosely bound primary particles) to form lacey soot, sometimes referred to as fractal soot, and compact soot particles of characteristic sizes of 100 s of nanometers [7,8]. Mature soot in common combustion systems typically grows to be outside the Rayleigh limit, so spectral absorption and scattering by soot particles has to be studied and determined empirically.

Studies have shown that the soot morphology, chemical composition, maturity, and soot mass or volume fraction affect the absorption and scattering properties. Radney et al. found that the absorption cross-section of soot was mostly consistent for lacey and compact soot particles within experimental uncertainty [8]. The extinction cross-section, however, was 33 % larger for compact soot relative to lacey soot of equivalent effective diameter, indicating that single scattering is still strongly dependent on particle shape. Furthermore, they showed that the extinction cross-section was more sensitive to soot mass than the absorption cross-section, indicating that for a larger volume fraction of soot, scattering plays a more dominant role in the extinction of radiation [8]. The widely cited Dalzell and Sarofim study found that the hydrogen to carbon ratio of the soot had significant impact on scattering and absorption capabilities, with an inversely proportional relationship between H/C ratio and scattering and absorption propensity [9]. Despite the large number of convolved factors that influence the extinction of radiation, the spectral dependence of extinction decays nearly monotonically for most combustion systems for wavelengths >300 nm. Below 300 nm, increased absorption in graphitic carbon is observed due to $\pi - \pi^*$ transitions and plasmon resonance [10]. A typical power-law fit of $K_\lambda = A \lambda^{-\beta}$, where A is a fit parameter (which has no wavelength dependence) and β is the experimental fit parameter, predicts the wavelength dependence of aerosolized soot particulate with reasonable accuracy. Values of β are nominally 1 within the Rayleigh limit, however soot measurements from some combustion systems have shown to deviate modestly, indicating that the power-law must be fit to determine the parameters A and β for unique systems [10].

Detonative systems differ from typical combustion scenarios in that there is an initial reaction, the detonation, and a subsequent reaction involving the fuel-rich post-detonation products, the fireball. The time-scales, temperatures, and pressures involved in detonation significantly change the soot characteristics. Several studies have investigated soot generated from explosive detonation, finding that there are both chemical and morphological differences compared to soot from conventional combustion systems [11–14]. Pantea et al. discovered that soot from explosive detonation had more nitrogen than carbon compared to reference soot samples, indicating that the explosive fuel type will impact the soot chemical composition and limit the application of hydrocarbon combustion soot optical properties to detonation systems [12]. Chen et al. compared soot from detonations from many explosives in different gas environments [14]. Environmental and charge conditions affected the soot chemical compositions, amount of soot produced, ultrafine diamond yield, grain size, and microstrain [14]. Pantea et al. proposed that the formation of diamond in soot is favored by the high temperatures and pressures, implying that the energetic output of an explosive changes the soot composition [12]. Greiner et al.

found that the soot produced in mixtures of TNT and RDX yield diamond spheroids and graphitic ribbons [11], and Chen et al. observed these in many explosive compositions [14]. The vast differences in soot produced by explosive detonation restricts the ability to apply trends in optical behavior found in soot formed in traditional hydrocarbon combustion systems. However, the results here suggest that the trends are more consistent with absorption and scattering than scattering alone, showing nearly monotonic increase in attenuation length with wavelength.

In the present study, significant laser absorption is apparent by the decreased spectral dependence on wavelength. However, due to experimental limitations (e.g. line-of-sight measurements, laser beam shielding [15]), power-law fits to the data might not be rigorously predictive, but rather will be a first order estimate for wavelength dependence in post-detonation fireballs. Future experiments to study post-detonation fireball absorption, scattering and overall extinction could help build a more predictive model for attenuation. Despite the overwhelming amount of research on optical properties of sooting flames in traditional hydrocarbon systems, there is a comparative lack of research on optical properties of soot from detonative systems. Parameters like explosive fuel type, soot mass, growth kinetics and pathways, chemical composition, and morphology on optical properties in explosive systems will help further elucidate not only the attenuation characteristics of which is concerned in the present study, but also emission characteristics, radiative heat transfer parameters, and cross-disciplinary explosive system modeling.

The explosive trends of optical attenuation length are best summarized by the time-average attenuation length after the period of early reactivity and high optical density. It is clearly visible in Figure 12 that attenuation lengths are

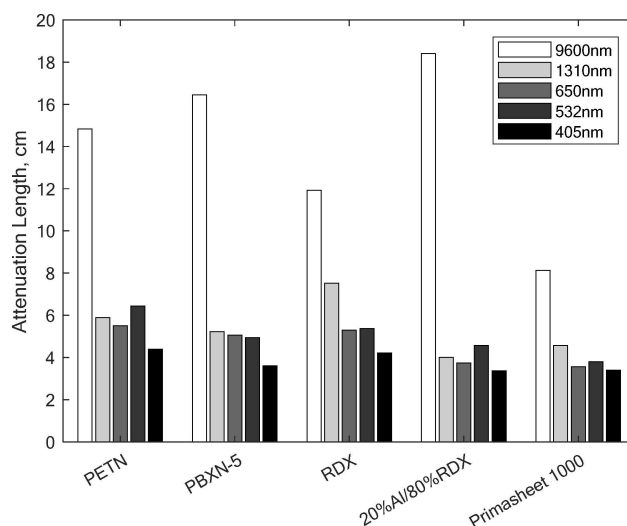


Figure 12. Mean attenuation length of each wavelength for all tested explosives.

considerably shorter for Primasheet 1000 relative to its constituents. Attenuation lengths are shorter for aluminized RDX compared to RDX, with PBXN-5 and PETN possessing even longer characteristic attenuation lengths. Long-wave infrared attenuation lengths are between a factor of 2.5 and 3 longer compared to the shorter wavelengths. Employing optical diagnostics in the long-wave infrared spectral region could produce higher fidelity data and would enable probing deeper into explosive fireballs relative to the visible and near-infrared wavelengths.

Mean attenuation lengths were calculated and are shown in Figure 13 for 6 RDX shots to show the reproducibility of the data. Error bars represent the standard error of measurement for $n=6$. The small standard error suggest that the data are fairly repeatable and attenuation length scales do not drift much shot-to-shot. The difference in standard error between wavelengths is likely attributable to the differences in signal-to-noise ratio for each laser-detector pair as well as beam chopping by large debris that is not replicable or controllable between shots.

Fireball scaling was employed to attempt to generalize these results to charges of different sizes. In our experiments, the fireball growth is limited by the chamber volume. Thus, by estimating the time for the fireball to fill the chamber, we can estimate the temporal range over which our results can be generalized to unconfined systems. Theoretical fireball diameter was calculated as a function of time using the relation [16]:

$$D(t) = C M^{\frac{5}{18}} t^{\frac{1}{3}} \quad (4)$$

Where diameter is in meters, M is the high explosive mass in kilograms, and time in seconds. C is a proportionality constant which can be determined by setting $D(t)$

equal to the maximum fireball diameter and t equal to the time at which the maximum diameter occurs. Using relations for maximum fireball diameter [17] and burn time [18]:

$$d = 3.30 M^{0.341} \quad (5)$$

$$t_c = 0.074 M^{\frac{1}{3}} \quad (6)$$

The equation becomes:

$$D(t) = 11.675 M^{\frac{5}{18}} t^{\frac{1}{3}} \quad (7)$$

Figure 14 shows the scaled fireball volume vs time. The 125 mg and 250 mg chamber volume-to-charge mass ratios are plotted against the scaled fireball growth rate. The intersection provides the point in time for which the fireball has expanded to the chamber volume. From Figure 14 it can be concluded that the in-fireball time scale for the 125 mg charge is 0–3 ms, while the in-fireball time scale for the 250 mg charge is 0–2 ms. During these times, the estimated unconfined fireball diameter is less than the chamber volume, and thus the local product concentrations can be assumed to be roughly the same as an unconfined system. After these times, since the products are not allowed to expand beyond the chamber, product concentrations are higher than unconfined fireballs, and attenuation lengths would be expected to be longer in unconfined explosion since it is free to expand fully.

Attenuation length will be constant for any volume of medium, provided the linear density of the media is constant. As explosive charge mass increases, the detonation pressure and temperature will remain constant despite an

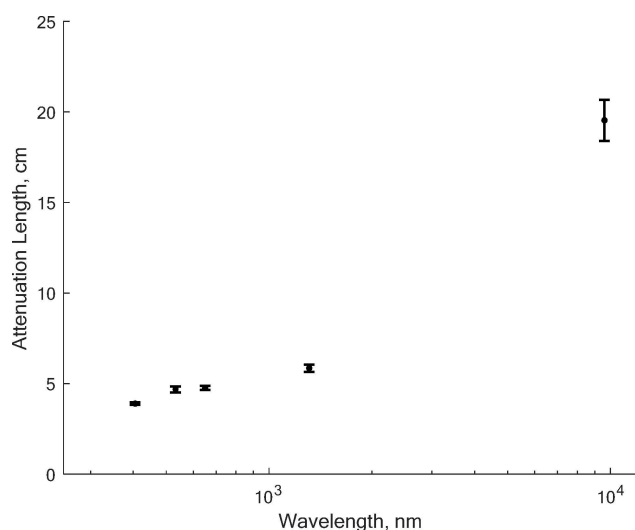


Figure 13. Mean attenuation length as a function of wavelength for 125 mg RDX charges ($n=6$).

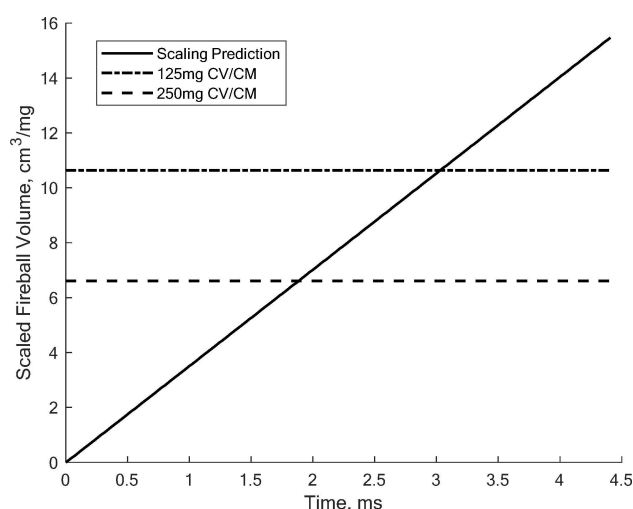


Figure 14. Scaled theoretical fireball volume as a function of time. Chamber volume to charge mass ratios are plotted for both 125 mg and 250 mg charges. Intersection locations represent the time at which the fireball fills the chamber volume.

increase in overall energy release. Thus, the composition of post-detonation combustion gases that fuel the fireball is expected not to deviate significantly as the charge is scaled from milligram scale to gram scale. However, the maximum diameter of the fireball and the timescales increase according to Eqs. 5 and 6. As fireball size increases with mass, the effective probe length through the fireball for optical diagnostics decreases.

Optical depth effects on measurements made in explosive fireballs can be mitigated by using small charge sizes, comparing explosive fireball diameter to the expected attenuation length, and utilizing explosives that burn more completely. Observing the wavelength dependence on optical attenuation length is important when considering extinction through the fireball. For shorter wavelengths, for example in the 400–500 nm range, the attenuation length is around 5 cm, which means that for charges greater than approximately 5 mg, measurements will be biased toward the outer region of the fireball and optical depth effects will be large. Conversely, the long-wave infrared attenuation length was approximately 20 cm, and would be less than the fireball diameter for charges up to 300 mg. Maintaining an attenuation length-to-fireball diameter ratio as close to 1 as possible is often desirable. Low opacity will ensure that the optical measurements made on the fireball are from the total volume of the fireball, rather than the outermost shell of the fireball. However, for most practical applications, explosive charges are much larger than those which allow for a 1:1 ratio with common wavelengths of interest, so optical measurements taken from outside the fireball are biased to the outer regions of the fireball on the order of the attenuation length for a given wavelength. Physical laser probes offer an alternative method for probing the internal dynamics of an explosive fireball of gram-scale or larger [19].

4 Conclusion

Temporally and spectrally resolved attenuation length measurements were made in explosive fireballs of five common high explosives: PETN, RDX, PBXN-5, Primasheet 1000, and an aluminized mixture of RDX, and for 125 mg and 250 mg charges. Visible through far-infrared laser light intensity was measured as a function of time for a period of 5 ms post-initiation of the high explosive. High-speed imaging showed the behavior of the fireball as well as determined the effects of laser beam steering during the event. Beam steering was deemed negligible since the laser beam did not deviate strongly from its starting position. Trends in both high explosive composition and wavelength on attenuation length were shown. Primasheet 1000 displayed the shortest attenuation length among tested explosives with average attenuation length of approximately 8 cm for the long-wave infrared and nearly 4 cm for visible through near-infrared. PETN was the least opaque high explosive fireball, with a mean long-wave infrared attenuation

length of 14 cm and a visible through near-infrared attenuation length between 4–6 cm. Aluminization of RDX decreased the attenuation length compared to the RDX without aluminum added, likely due to the enhanced combustion effects generated by the aluminum particulate inside the fireball. The HMX-based PBXN-5 explosive had modestly longer attenuation length compared to RDX and the aluminized RDX, despite have equivalent oxygen balance.

In general, the long-wave infrared laser light attenuation length was significantly longer relative to the near-infrared and visible wavelengths studied, often by a factor of 2.5 to 3. Visible and near-infrared laser light was attenuated much more severely, with the attenuation length being smaller than the fireball diameter for the entire event. The long-wave infrared laser light was attenuated significantly less, having attenuation lengths longer than the fireball diameter for the majority of the event. For the first 500 μ s, the attenuation length was approximately equal to the fireball diameter. Scaling the charge size up from 125 mg to 250 mg did not dramatically change the attenuation length measured during the period of fireball luminosity. However, after the combustion of the fireball, the attenuation length was modestly decreased. Laser attenuation departed from the scattering-predicted λ^{-4} , indicating that significant absorption was present in addition to scattering. Further study of detonation soot optical properties is likely required to develop predictive models for spectral extinction for a given explosive, charge size and chamber volume.

Fireball size scaling arguments were made in attempt to generalize the results. Attenuation length is not unique for any specific charge size, rather it is specific for a given explosive, wavelength, and fireball volume before it expands to the confinement volume. For our purpose, it can also be understood as the maximum diameter of fireball a beam of light can encounter for which the optically thin approximation is likely applicable. As the fireball diameter increases, the ratio of attenuation length-to-fireball diameter decreases, and the observer measures increasingly smaller portions of the fireball. Fireballs from gram-scale and larger explosive charges likely present attenuation lengths greater than the fireball diameters for wavelengths of interest, from the visible through long-wave infrared.

Acknowledgements

This research was supported by the Defense Threat Reduction Agency (DTRA). The program manager is Dr. Allen Dalton. The views expressed in this manuscript are those of the authors and do not necessarily represent the views of DTRA or the University of Illinois.

References

- [1] N. Glumac, H. Krier, P. Lynch, J. Mott Peuker, Optical Spectroscopy of Fireballs from Metallized Reactive Materials, **2013**, 1.
- [2] W. K. Lewis, C. G. Rumchik, M. J. Smith, Emission spectroscopy of the interior of optically dense post-detonation fireballs, *J. Appl. Phys.* **2013**, 113, 24903.
- [3] J. R. Carney, J. S. Miller, J. C. Gump, G. I. Pangilinan, Time-resolved optical measurements of the post-detonation combustion of aluminized explosives, *Rev. Sci. Instrum.* **2006**, 77, 063103.
- [4] J. M. Peuker, P. Lynch, H. Krier, N. Glumac, Optical depth measurements of fireballs from aluminized high explosives, *Opt. Lasers Eng.* **2009**, 47, 1009–1015.
- [5] P. W. Cooper, *Explosives Engineering*, Wiley-VCH, Weinheim, Weinheim, **1996**.
- [6] R. K. Hanson, R. M. Spearrin, C. S. Goldenstein, *Spectroscopy and Optical Diagnostics for Gases*. Springer International Publishing Switzerland, **2016**.
- [7] H. A. Michelsen, Probing soot formation, chemical and physical evolution, and oxidation: A review of in situ diagnostic techniques and needs, *Proc. Combust. Inst.* **2017**, 36, 717–735.
- [8] J. G. Radney, R. You, X. Ma, J. M. Conny, M. R. Zachariah, J. T. Hodges, C. D. Zangmeister, Dependence of soot optical properties on particle morphology: Measurements and model comparisons, *Environ. Sci. Technol.* **2014**, 48, 3169–3176.
- [9] W. H. Dalzell, A. F. Sarofim, Optical Constants of Soot and Their Application to Heat-Flux Calculations, *J. Heat Transfer* **1969**, 91, 100–104.
- [10] A. Bescond, J. Yon, F. X. Ouf, C. Rozé, A. Coppalle, P. Parent, D. Ferry, C. Laffon, Soot optical properties determined by analyzing extinction spectra in the visible near-UV: Toward an optical speciation according to constituents and structure, *J. Aerosol Sci.* **2016**, 101, 118–132.
- [11] N. R. Greiner, D. S. Phillips, J. D. Johnson, F. Volk, Diamonds in detonation soot, *Nature* **1988**, 333, 440–442.
- [12] D. Pantea, S. Brochu, S. Thiboutot, G. Ampleman, G. Scholz, A morphological investigation of soot produced by the detonation of munitions, *Chemosphere* **2006**, 65, 821–831.
- [13] V. L. Kuznetsov, A. L. Chuvilin, E. M. Moroz, V. N. Kolomiichuk, S. K. Shaikhutdinov, Y. V. Butenko, I. Y. Mal'kov, Effect of explosion conditions on the structure of detonation soots: Ultra-disperse diamond and onion carbon, *Carbon N. Y.* **1994**, 32, 873–882.
- [14] P. Chen, F. Huang, S. Yun, Characterization of the condensed carbon in detonation soot, *Carbon N. Y.* **2003**, 41, 11, 2093.
- [15] J. Zhu, M. U. N. Y. Choi, G. W. Mulholland, S. L. Manzello, L. A. Gritzo, J. Suoanttila, Measurement of Visible and Near-IR Optical Properties of Soot Produced From Laminar Flames, **2002**, 29, 2367.
- [16] H. C. Hardee, D. O. Lee, W. B. Benedick, Thermal Hazard from LNG Fireballs, *Combust. Sci. Technol.* **1978**, 17, 189–197.
- [17] J. B. Gayle, J. W. Bransford, G. C. Marshdl, Size and duration of fireballs from propellant explosions, *NASA Tech. Memo.* **1965**, X-53314.
- [18] S. M. Gilbert, A model for the effects of a condensed phase explosion in a built-up area, Loughborough University, **1994**.
- [19] C. Murzyn, A. Sims, H. Krier, N. Glumac, High speed temperature, pressure, and water vapor concentration measurement in explosive fireballs using tunable diode laser absorption spectroscopy, *Opt. Lasers Eng.* **2018**, 110, 186–192.

Manuscript received: July 1, 2019

Revised manuscript received: October 3, 2019

Version of record online: November 5, 2019